

# Ferrocenyl–Triphenyltin Complexes as Lysosome-Targeted Imaging and Anticancer Agents

Juanjuan Li,<sup>†</sup> Xicheng Liu,<sup>\*,†</sup> Haifeng Zhang,<sup>‡</sup> Xingxing Ge,<sup>†</sup> Yanhua Tang,<sup>†</sup> Zhishan Xu,<sup>†,§</sup> Laijin Tian,<sup>†</sup> Xiangai Yuan,<sup>†</sup> Xudong Mao,<sup>†</sup> and Zhe Liu<sup>\*,†</sup>

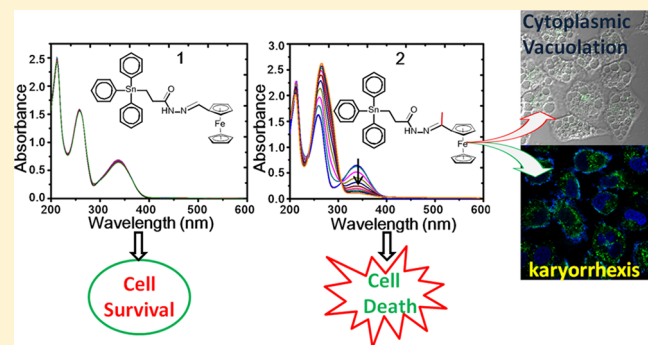
<sup>†</sup>Institute of Anticancer Agents Development and Theranostic Application, The Key Laboratory of Life-Organic Analysis and Key Laboratory of Pharmaceutical Intermediates and Analysis of Natural Medicine, School of Chemistry and Chemical Engineering, Qufu Normal University, Qufu 273165, China

<sup>‡</sup>Department of Chemistry and Chemical Engineering, Jining University, Qufu 273155, China

<sup>§</sup>Department of Chemistry and Chemical Engineering, Shandong Normal University, Jinan 250014, China

## Supporting Information

**ABSTRACT:** In this paper, two ferrocenyl–triphenyltin complexes were synthesized and characterized. Complex 2 is constructed as new multifunctional therapeutic platform for lysosome-targeted imaging and displayed much higher cytotoxicity than its analogue 1 by the introduction of a methyl group instead of a hydrogen atom in acylhydrazone. The cyclic voltammograms and reaction with GSH (glutathione) further confirmed that complex 1 has a reversible redox peak and can react with GSH, which indicate that complex 1 might lose its anticancer effect by undergoing reaction with GSH once it enters the cancer cell. Complex 2 could effectively catalyze the oxidation of NADH (the reduced form of nicotinamide adenine dinucleotide) to NAD<sup>+</sup> and induce the production of reactive oxygen species (ROS), lead to caspase-dependent apoptosis through damaged mitochondria, simultaneously, accounting for the mitochondrial vacuolization and karyorrhexis. The caspase-3 activation and cytoplasmic vacuolation karyorrhexis induced by complex 2 revealed that the A549 cell lines might undergo cell death primarily mediated by apoptosis and oncosis; however, 1 cannot reproduce this effect. Taken together, these results indicated that complex 2 has more potential for evolution as a new bioimaging and anticancer agent.



## INTRODUCTION

Medicinal application of ferrocene derivatives has been an active research area in the last few decades. Many reports have shown that ferrocene derivatives are highly active against several diseases whether *in vitro* or *in vivo*, including fungal and bacterial infections,<sup>1,2</sup> malaria,<sup>3</sup> human immunodeficiency virus (HIV),<sup>4</sup> and cancer.<sup>5</sup> The anticancer potency of simple ferrocene derivatives was generally low; however, the incorporation of the ferrocene group into other transition metal anticancer complexes, such as platinum, ruthenium, iridium, copper, and gold complexes, among others, could effectively enhance their anticancer activity.<sup>6</sup> Little efforts have been put forward to design the combination of ferrocene with organotin.

Organotin complexes play important roles in biological activities and human health, and a large number of organotin complexes have shown anticancer activity higher than that of the widely used anticancer drug cisplatin *in vitro*.<sup>7–9</sup> It is well-known that the biochemical activity of organotin complexes is influenced greatly by the type of groups in the organotin moiety and the number of Sn–C bonds.<sup>10</sup> By tackling these

factors, the toxic side effects of organotin complexes could be decreased. Previous studies have shown that the toxic side effects could be decreased by increasing the numbers of alkyl substituents on the tin atom to a certain extent or using an alkyl with a long carbon chain to replace the smaller one, such as butyl, phenyl, benzyl, cyclohexyl, and so on.<sup>11</sup>

Recent studies showed that classic molecule assembly of NADH (reduced form of nicotinamide adenine dinucleotide) and NAD<sup>+</sup> lies in various biological processes, including calcium homeostasis, immunological functions, energy metabolism, antioxidation/generation of oxidative stress, mitochondrial functions, and so on,<sup>12–16</sup> which have been extensively studied in the field of cell death.<sup>17–19</sup> NAD<sup>+</sup> and NADH could adjust various significant factors in cell death, for example, poly(ADP-ribose) polymerase-1 (PARP-1), mitochondrial permeability transition, and apoptosis-inducing factor. Simultaneously, NADH-dependent reactive oxygen species (ROS) generation from mitochondria is one of critical oxidation

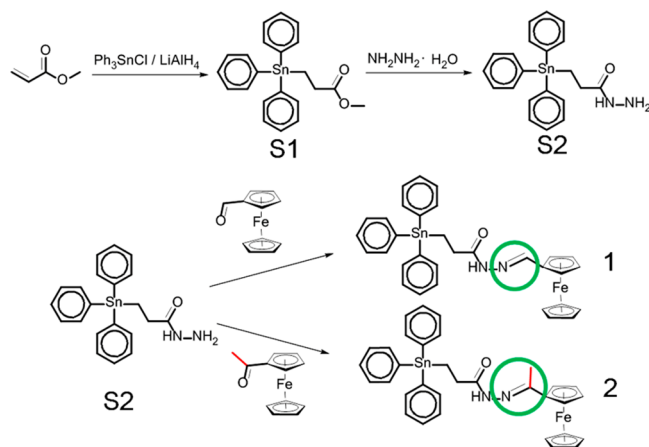
**Received:** November 27, 2018

mechanisms of anticancer. In addition, numerous studies have shown that transition metal anticancer complexes, such as iridium and ruthenium, can catalyze the change of NADH to NAD<sup>+</sup>, lead to the production of ROS, and eventually induce apoptosis.<sup>20,21</sup>

Molecular imaging of drugs in cells plays a crucial role in comprehending their mechanism of action in many significant cellular processes, such as real-time tracking of drug intracellular transport and monitoring the interactions between the drug and the biological target molecule. However, the luminescent properties of organotin complexes are rarely studied. Also, the development of anticancer complexes for organelle-specific attack has attracted much attention. Delivering drugs to organelle-specific sites can effectively increase drug concentration at the target sites and reduce side effects.<sup>22,23</sup> Now, targeting of the lysosomes has appeared as an effective means for anticancer therapy due to the ability of degradation proteins and other cellular organelles.<sup>24</sup> Groups such as those of Mokhir, Chao, and O'Shea have developed metal complexes and organic compounds as lysosome-tracking reagent and therapeutic agent.<sup>25–27</sup>

Inspired by these results, herein, a ferrocene molecule was introduced into the alkyl chain of triphenyltin through the acylhydrazone group to increase the length of carbon chain and the volume of tin complexes. Two iron–tin heteronuclear metal anticancer complexes were synthesized, and the designed strategy of target complexes was shown in Scheme 1. It is

### Scheme 1. Design Strategy of Ferrocenyl–Triphenyltin Complexes



interesting that the introduction of a methyl group in acylhydrazone in complex 2 significantly enhanced anticancer activity. In addition, we investigated the mechanism of action and evaluated the imaging capabilities of iron–tin heteronuclear complexes.

## RESULTS AND DISCUSSION

Starting  $\beta$ -methoxycarbonyl ethyl triphenyltin **S1** (Scheme 1) was prepared according to the previously published procedure.<sup>28</sup> Subsequently, synthesis of **S2** by was achieved with **S1** and commercially available hydrazine hydrate. Complexes **1** and **2** were obtained by the reaction of  $\beta$ -hydrazinocarbonyl ethyl triphenyltin **S2** and ferrocene derivatives, and heating at reflux for 24 h under nitrogen atmosphere. The crude products were purified by slow diffusion of hexane into saturated dichloromethane solutions of **1** and **2** at room temperature,

and red block-shaped single crystals of **1** are also obtained (CCDC 1843945). The asymmetric unit molecular structure of complex **1** is shown in Figure 1. Crystal data are listed in Table S1, and selected bond lengths and angles are listed in Tables S2, consistent with the expected structure.

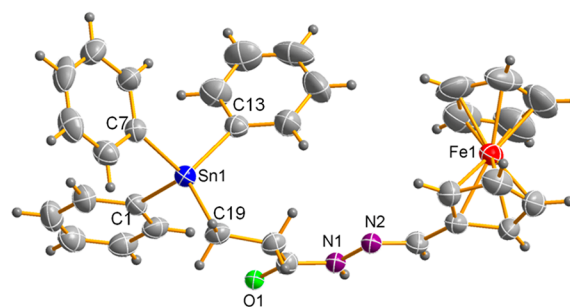


**Figure 1.** Asymmetric unit molecular structure with atom numbering schemes for **1**.

The stability of complexes under aqueous and physiological conditions is one of the most crucial factors in assessing their applications in the body. Therefore, the stability of as-synthesized complexes (**1** and **2**) in 40% MeOH/60% H<sub>2</sub>O (*v/v*) was monitored by ultraviolet–visible (UV–vis) spectrum at 298 K (Figure S1). There is no change for the complexes within 8 h, which indicates that target complexes have excellent stability under the test conditions. A high level of reduction for glutathione (GSH,  $1 \times 10^{-3}$ – $10 \times 10^{-3}$  M) is one of the biochemical characteristics of malignant tumor.<sup>29</sup> On the basis of these physiological characteristics, the stabilities of complexes **1** and **2** in 20% MeOH/80% PBS (*v/v*, phosphate buffer solution) containing 1 mM GSH was studied. Interestingly, as shown in Figure S2, complex **1** exhibited an increased absorption after incubation with  $1 \times 10^{-3}$  M GSH compared with the result in water. However, complex **2** remained stable under the test conditions within 18 h, which manifests the high stability of complex **2** in physiological systems outside the tumor sites. Therefore, the instability with GSH may lead to the loss of anticancer activity for complex **1**.

Next, the redox properties of **1** and **2** were investigated by the cyclic voltammetry that performed with two consecutive scans from  $-1.0$  to  $+1.0$  V. Very different electrochemical characteristics were observed for complexes **1** and **2**. For **1**, reversible redox processes were found to give a very strong cathodic peak at  $+0.222$  V and an anodic peak at  $+0.128$  V; however, no obvious redox processes appeared for complex **2** (Figure 2). The results of cyclic voltammograms lead us to further speculate that complex **1** has favorable redox property,

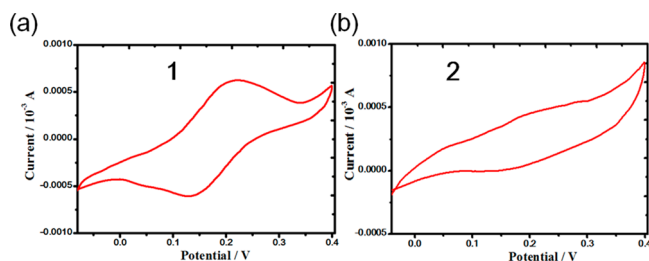


**Figure 2.** Evaluation of the cyclic voltammograms of **1** and **2** (1 mM) in anhydrous DMSO solutions, scan rate = 100 mV/s.

**Table 1.** Inhibition of Growth of Cancer Cells by **1**, **2**, and Cisplatin Recorded over a Period of 24 h and log *P* for Complexes **1** and **2**

complex	IC <sub>50</sub> (μM)				log <i>P</i> <sup>a</sup>
	A549	HeLa	HepG2	GL261	
<b>1</b>	>100	67.0 ± 6.3	69.4 ± 9.6	30.0 ± 7.9	2.5 ± 0.5
<b>2</b>	1.4 ± 0.3	1.4 ± 0.7	3.2 ± 0.4	2.5 ± 0.7	3.4 ± 0.3
cisplatin	21.3 ± 1.7	7.5 ± 0.2	20.9 ± 1.2	15.4 ± 0.5	

<sup>a</sup>Results are the means of three independent experiments.

which might lose anticancer efficacy by reaction with GSH once it enters the cancer cell.

We evaluated the effects of cytotoxicity for **1** and **2** in vitro against the viability of A549 (human lung cancer cells), HeLa (human cervical cell cancer), HepG2 (human hepatoma cell), and GL261 (mouse glioma cells) by MTT assay after 24 h. The half-maximal inhibitory concentration (IC<sub>50</sub>) values are listed in Table 1. Complex **2** is significantly more active than either cisplatin or **1** in all the cells tested, and **1** has only slightly antiproliferative effects on GL261 cells. Complex **2** displays cytotoxicity against A549 cells, with an IC<sub>50</sub> value of 1.4 ± 0.7 μM, up to a 15-fold increase compared with that of cisplatin (IC<sub>50</sub>: 21.3 ± 1.7 μM). Interestingly, the anticancer activity of complex **2** was significantly increased in all the cells tested by simply replacing a hydrogen atom by a methyl group in the acylhydrazone group of **1**. L1 and L2 (Scheme S1) are the analogues of complexes **1** and **2** but without the triphenyltin unit; S2 is an analogue of as-synthesized complexes but without the ferrocene unit. As shown in Table S3, the lower antiproliferative activities of L1, L2, and S2 indicate the integrations of triphenyltin, ferrocene derivative, and acylhydrazone cause favorable antiproliferative activity for complex **2**. Lipophilicity is one of the significantly factors which would affect the cytotoxic potency and cellular uptake levels of the drugs. The lipophilicity of complexes could be evaluated by the value of log *P* (partition coefficient in oil/water). The log *P* values of **1** and **2** were 2.5 ± 0.5 and 3.4 ± 0.3 respectively (Table 1), which show that the higher the lipophilicity for complex **2**, the better the cytotoxic activity. Next, the antiproliferative activities of **1** and **2** against BEAS-2B (human bronchial epithelial normal cell) were evaluated by MTT assay after 72 h incubation; unfortunately, no obvious selectivity was observed for complexes **1** and **2**.

Biological processes including energy metabolism, cell death, and mitochondrial function are regulated by NAD<sup>+</sup> or NADH in some manners.<sup>30</sup> It has been demonstrated that Ir<sup>III</sup> and Ru<sup>II</sup> cyclopentadienyl complexes can be used as highly effective catalyst to convert the coenzyme NAD<sup>+</sup>/NADH couple through transfer hydrogenation reactions. We used UV-vis and NMR to define the contributions of **1** and **2** to catalyze NADH to NAD<sup>+</sup>, as shown in Figures 3 and S3. NADH was incubated in the same solution (50% MeOH/50% H<sub>2</sub>O (v/v)) as control (Figure S4). The conversion of NADH to NAD<sup>+</sup> was evaluated based on the fact that NADH has a UV absorption at 339 nm while NAD<sup>+</sup> does not. Subtracting the effects of control, the turnover numbers (TONs) of **2** (84.0) were calculated at 340 nm. Almost no conversion was detected for **1**, suggesting complex **2** had a strong catalytic ability of to convert the coenzyme NAD<sup>+</sup>/NADH couple, but that complex **1** did not. Due to the push-electron effect of the methyl group, the electron cloud density of C=N increased; therefore, the activity is strengthened. The charge of C (C=N) is +0.246 for complex **2**, about 5 times higher than that of **1** (+0.049, Figure

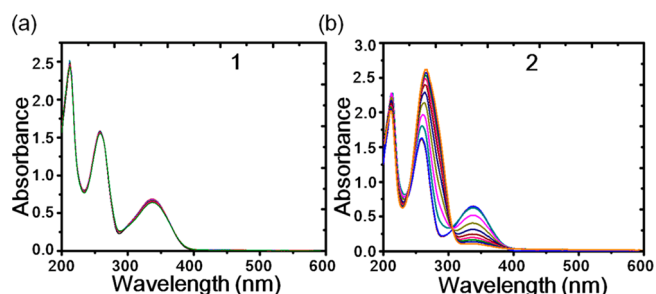


**Figure 3.** UV-vis spectra of the reaction of NADH (100 μM) in 50% MeOH/50% H<sub>2</sub>O (v/v) at 298 K for 9 h. (a) **1** (1 μM); (b) **2** (1 μM).

S5). The positive charge of the carbon makes the hydride transfer from the coenzyme NADH reaction more active.

Subcellular localization of **1** and **2** was easily determined by confocal microscopy in A549 cells on account of their intrinsic luminescence, which can provide more hints for the mechanisms of anticancer (Figure 4). The results show that

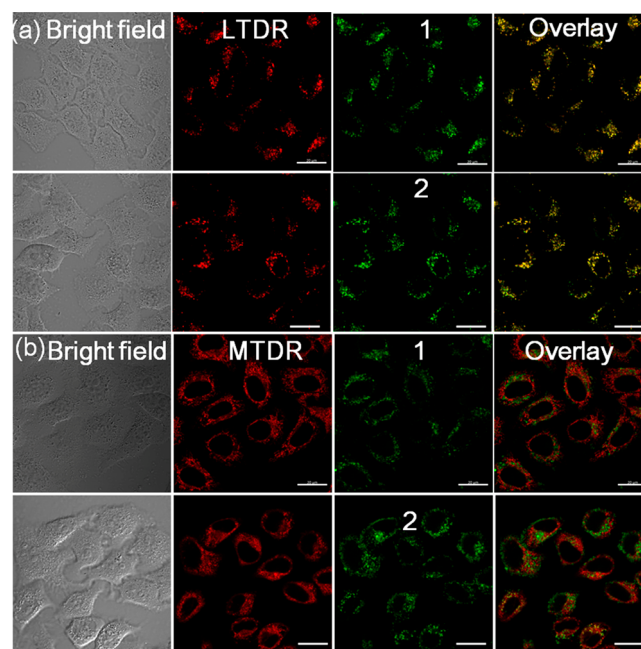


**Figure 4.** (a) Confocal microscopy images of A549 cells co-labeled with **1** (10 μM, 0.5 h) and **2** (IC<sub>50</sub> = 1.4 μM, 0.5 h) and LTDR (100 nM, 0.5 h); (b) Confocal microscopy images of A549 cells co-labeled with **1** (10 μM, 0.5 h) and **2** (1.4 μM, 0.5 h) and MTDR (75 nM, 0.5 h). The excitation and emission bands were as follows: for complexes: λ<sub>ex</sub> = 488 nm, λ<sub>em</sub> = 520 ± 30 nm; for MTDR: λ<sub>ex</sub> = 644 nm, λ<sub>em</sub> = 700 ± 30 nm; for LTDR: λ<sub>ex</sub> = 594 nm, λ<sub>em</sub> = 630 ± 30 nm. Scale bar: 20 μm.

**1** and **2** specifically targeted lysosomes with high Pearson's colocalization coefficients (PCC) of 0.90 and 0.92, respectively, indicating the complexes both are able to stain lysosomes specifically and possess lysosome-targeting specificity in A549 cells. However, minimal overlap with MTDR (mitochondria specific probe) is observed for **1** (PCC = 0.04) and **2** (PCC = 0.06) (Figure 4b). Selective accumulation of the **1** and **2** in cancer cells is of great concern for targeted cancer therapy.<sup>31</sup>

Excessive generation of ROS and lysosomal permeability is often triggered by the disruption of the lysosomal integrity.<sup>32,33</sup> To investigate whether lysosomal damage induced by **1** and **2** was accompanied by lysosome-targeting specificity, lysosomal integrity of A549 cells was evaluated after treatment with **1** (10  $\mu\text{M}$ ) and **2** (1.4  $\mu\text{M}$ ,  $\text{IC}_{50}$ ) at 1, 6, and 17 h by acridine orange (AO) staining. AO exhibits red fluorescence when accumulated in lysosomes and green fluorescence when bound to RNAs in the nuclei and cytosol. As shown in Figure 5, red

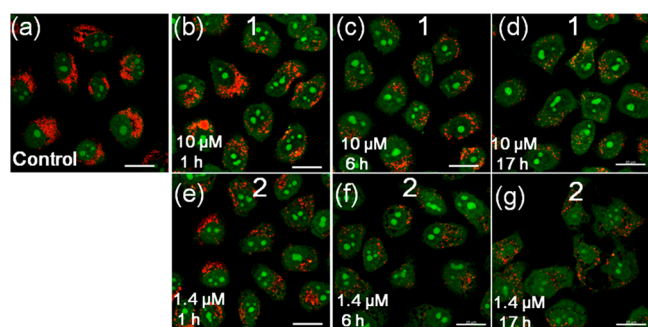


**Figure 5.** Observation of lysosomal disruption in A549 cells caused by **1** (10  $\mu\text{M}$ ) and **2** (1.4  $\mu\text{M}$ ) and stained by AO (5  $\mu\text{M}$ , 15 min).  $\lambda_{\text{ex}}$  = 488 nm,  $\lambda_{\text{em}}$  = 510  $\pm$  20 nm;  $\lambda_{\text{em}}$  = 625  $\pm$  20 nm. The cells were treated with (a) control, (b) **1** (10  $\mu\text{M}$ ) 1 h, (c) **1** (10  $\mu\text{M}$ ) 6 h, (d) **1** (10  $\mu\text{M}$ ) 17 h, (e) **2** (1.4  $\mu\text{M}$ ) 1 h, (f) **2** (1.4  $\mu\text{M}$ ) 6 h, (g) **2** (1.4  $\mu\text{M}$ ) 17 h. Scale bar: 20  $\mu\text{m}$ .

fluorescence basically disappears from the lysosome when exposed to complexes **1** (10  $\mu\text{M}$ ) and **2** (1.4  $\mu\text{M}$ ) after 1 h versus control, and obvious lysosomal damage was found after 17 h.

To assess the mechanism of cell death in A549 cells induced by **1** and **2**, we evaluated the cytotoxicity in the presence of different chemical inhibitors to adjust canonical form of cell death. The cells were treated with necroptosis inhibitor necrostatin-1 (Nec-1), autophagy inhibitor 3-methyladenine (3-MA), the protein synthesis inhibitor cycloheximide (CHX), and the protease inhibitor leupeptin (LPT) (Table S4). The data analysis indicates the cytotoxic effects of **1** and **2** did not demonstrate significantly change, suggesting that these inhibitors are not operative.

Apoptosis is one of the canonical forms of cell death.<sup>34</sup> In order to further insight into whether **1** and **2** inhibited cancer cells growth via inducing apoptosis, A549 cells were exposed to **1** and **2** at different concentrations including 0.7, 1.4, 2.8, and 4.2  $\mu\text{M}$  for 24 h and analyzed by flow cytometry. As shown in Figure 6 and Table S5, almost no apoptosis was induced by **1** even at very high concentrations of 4.2  $\mu\text{M}$ , and 91.8% of cells remained viable. However, for complex **2**, about 68.6% of the A549 cells were undergoing apoptosis after 24 h at the concentration of 4.2  $\mu\text{M}$  (including 42.9% of cells in late apoptosis), while the 92.8% of untreated cells remained viable under the same conditions.

Studies have confirmed that NADH depletion is an early event in apoptosis and could mediate cellular energy metabolism, which is a significant factor to decide cell death patterns.<sup>17,35</sup> To assess whether complex-induced apoptosis is caused by depletion of NADH in cells, we added additional NADH when testing for apoptosis. In the presence of additional NADH, complex **2** appeared to lower the cell death of human A549 cancer cells to a certain degree compared to untreated-NADH cells (Figure S6 and Table S6). As shown, about 69.4% of the treated-NADH A549 cells were viable; however, about 31.4% were viable when only treated by complex **2** at a concentration of 4.2  $\mu\text{M}$ . The higher

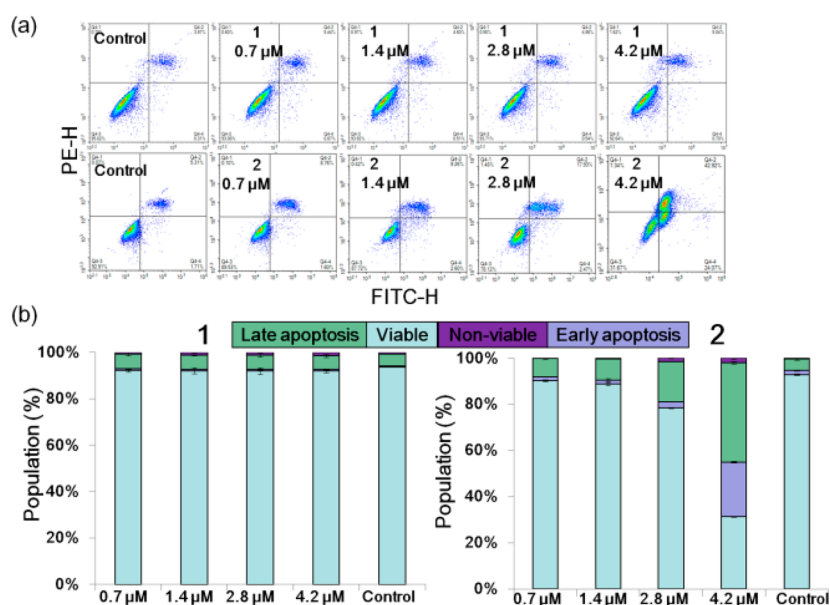


**Figure 6.** Flow cytometry detected apoptosis based on annexin V and PI staining of A549 cells treated with **1** and **2** after 24 h at 310 K. (a) Populations for cells treated by **1** and **2**. (b) Histogram for A549 cells treated with different concentrations of **1** and **2** for 24 h.

cell viability indicated that the presence of additional NADH obviously protected the cells from the attack of complex 2, thus showing that depletion of NADH has a critical function in inducing apoptosis.

The intrinsic pathway of apoptosis is regulated by mitochondria through the release of proapoptotic proteins from mitochondria to activate caspases (death-driving proteolytic proteins).<sup>36</sup> Caspase-3 is an important biomarker of apoptosis which has been identified as a key performer of apoptosis in mammalian cells.<sup>37</sup> The activation of caspase-3 in A549 cells was verified using the Caspase-Glo assay which was operated to elucidate the effects of 1 and 2 on caspase-3 activity. As shown in Figure 7 and Table S7, for complex 2, an

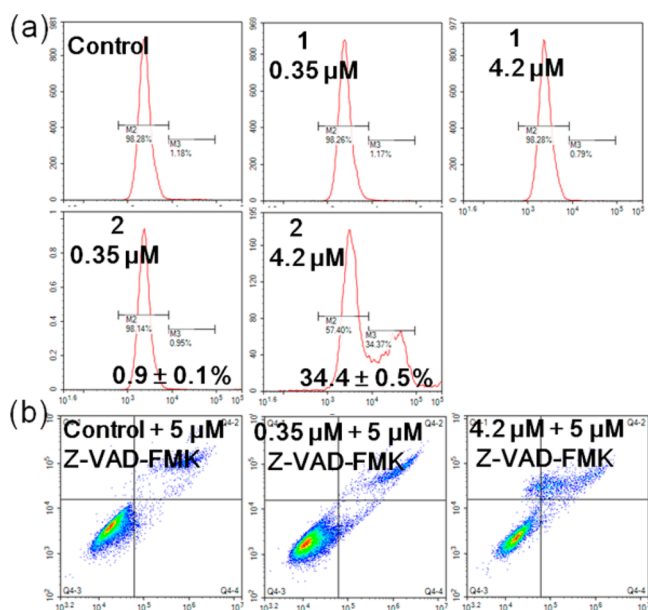


**Figure 7.** Detection of caspase-3 activity in A549 cells after the cells were treated with different concentrations of 1 and 2. (a) FL2 histogram the populations of cells in activated caspase-3 after treatment of different concentrations of 1 and 2 for 24 h. Data are quoted as mean  $\pm$  SD of three replicates. (b) Flow cytometry detected apoptosis based on Annexin V/PI assay of A549 cells treated with 2 and the pan-caspase inhibitor Z-VAD-FMK for 24 h.

increase in caspase-3 activity of about 29-fold was observed, compared with that of control, and the activation of caspase-3 was caused in a dose-dependent manner. However, the activation of caspase-3 induced by 1 is not observed (Figure 7a). Next, the apoptosis caused by 2 was efficiently held back when adding the caspase inhibitor z-VAD-fmk (5  $\mu\text{M}$ ); the cell viability remains above 80% (Figure 7b and Table S8).

Oncosis is different from apoptosis in morphological changes, which might hold the key of overcoming drug-resistance in cancer therapy. Oncosis is characterized by a series of defined morphological events, such as cytoplasmic vacuolation, karyorrhexis, or even dissolution, and mitochondrial swelling.<sup>38,39</sup> As shown in Figure 4, weak cytoplasmic vacuolation and solid granules have been induced by 2 at 1.4  $\mu\text{M}$  after 0.5 h as shown in confocal microscopy images of A549 cells; however, this result was not observed with 1. To gain more insights into the intracellular effects of 2, the mitochondria and nuclear morphological changes were further studied using confocal microscopy. Substantial morphological changes including cytoplasmic vacuolation and partial

karyorrhexis were observed by 2 at 4.2  $\mu\text{M}$  after 0.5 h (Figures 8a and S7). In a time- and dosage-dependent manner a large

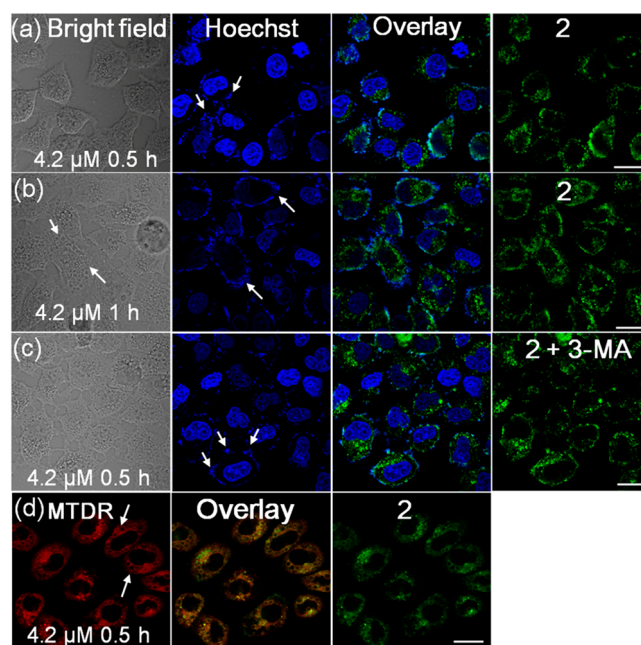


**Figure 8.** Representative confocal microscopy images showing the morphological features of A549 cells treated with 2 at 4.2  $\mu\text{M}$  for 0.5 and 1 h. (a) 2 4.2  $\mu\text{M}$ , 0.5 h, (b) 2 4.2  $\mu\text{M}$ , 1 h, (c) 2 4.2  $\mu\text{M}$ , 0.5 h and 3-MA, (d) co-labeled with 2 (4.2  $\mu\text{M}$ , 0.5 h) and MTDR (75 nM, 0.5 h). The excitation and emission bands were as follows: for complex:  $\lambda_{\text{ex}} = 488$  nm,  $\lambda_{\text{em}} = 520 \pm 30$  nm; for Hoechst:  $\lambda_{\text{ex}} = 405$  nm,  $\lambda_{\text{em}} = 450 \pm 30$  nm; for MTDR:  $\lambda_{\text{ex}} = 644$  nm,  $\lambda_{\text{em}} = 700 \pm 30$  nm. Scale bar: 20  $\mu\text{m}$ .

number of karyorrhexis appeared and scattered in the cytoplasm accompanied by serious cytoplasmic vacuolation. The autophagy inhibitor 3-methyladenine (3-MA) was used to prove whether cell vacuolization was caused by autophagy; the result showed the cytoplasmic vacuolation induced by 2 in A549 cells was not influenced by 3-MA, hinting a pathway different from the autophagy process (Figure 8c). Hollow spheres of abnormal morphology represent the extremely swollen and damaged mitochondria in most cells, suggesting mitochondria dysfunction.<sup>40</sup> After 0.5 h of incubation of A549 cells with 2 (4.2  $\mu\text{M}$ ), the morphological changes were observed by damaged mitochondria, Figure 8d. Co-localization analysis of 2 and MTDR gives proof that most mitochondria show hollow spheres, representing the extremely swollen mitochondria. Mitochondria dysfunction mediated forms of cell death are characterized by these morphological changes.

Increased mitochondrial membrane permeability in extremely swollen and damaged mitochondria of A549 cells are regarded as early events.<sup>36</sup> The loss of mitochondrial membrane potential (MMP) induced by 1 and 2 can be assessed by detecting the decrease in red fluorescence and increased green fluorescence using JC-1 and flow cytometry. At the indicated concentrations, 2 displayed a significant concentration-dependent increase with a remarkable loss of MMP, e.g., from 8.7% (control) to 32.9% (2.8  $\mu\text{M}$ ); however, 1 caused negligible impact on the MMP level (Figure 9a and Table S9). Studies have shown that the reductive coenzyme of cytosolic NADH could be directly transferred to oxygen in the mitochondria with the generation of electrochemical mem-

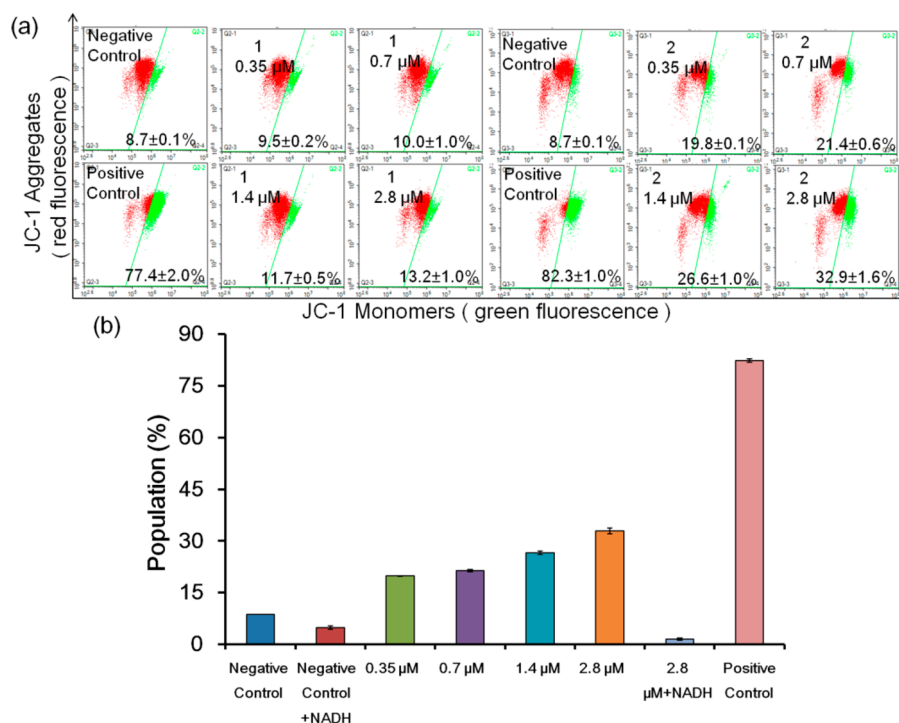


**Figure 9.** (a) Representative histograms for the analysis of MMP by flow cytometry using the JC-1 dye. The red aggregates and green monomers are gated. (b) MMP is analyzed by flow cytometry in A549 cancer cells treated with complex 2 at different concentrations and complex 2 in the presence of NADH (400 µg/mL) at 2.8 µM. Data are quoted as mean ± SD of three replicates.

brane potential under certain conditions, which are mediated by cytosolic cytochrome c and mitochondrial cytochrome oxidase.<sup>41,42</sup> Complex 2 may break this process by consuming NADH in the cell, causing a decrease in MMP. Therefore, we add NADH to the cell solution containing complex 2 at a concentration of 2.8 µM, which only causes 1.5% of cells to lose MMP. As shown in Figures 9b and S8 and Table S10, the lower loss of MMP in NADH-treated cells indicated that exogenous NADH effectively prevents the increase of mitochondrial membrane permeability induced by complex 2.

Meanwhile, NAD may also affect the antioxidation and generation of oxidative stress through several pathways.<sup>12</sup> The capability of mitochondrial oxidative stress for 1 and 2 was detected using DCFH-DA fluorescence assay by flow cytometry analysis. As shown in Figure S9 and Table S11, ROS generated in A549 cells exhibit the concentration-dependent increase for complex 2, but 1 did not observe any change. At 2.8 µM, complex 2 displayed a very strong ROS-inducing ability compared with that of negative control. However, for complex 1, almost no change occurred even at 2.8 µM, which showed that ROS contributes to cell death of A549 cells. The ROS generation can cause cell death through mitochondria dysfunction and autophagic vacuole accumulation.<sup>43</sup> The previous study showed that xanthine oxidase/xanthine dehydrogenase could induce the generation of ROS by oxidizing NADH.<sup>44,45</sup> To probe the oxidizing capacity of the generation of ROS, A549 cancer cells were pretreated with NADH (400 µg/mL) before the addition of complex 2 (Figures 10 and S10 and Table S12). Compared with the result without NADH, a certain degree of decrease in the generation ROS was observed for cells pretreated with NADH for 2 at the concentration of 2.8 µM. It maybe due to excessive NADH consuming the ROS produced by complex 2.

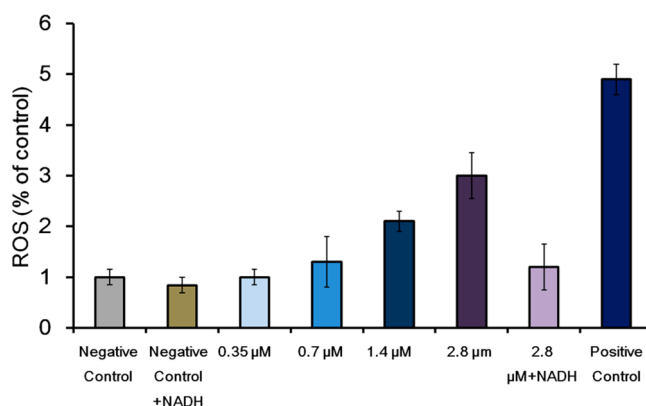


**Figure 10.** ROS induction analyzed by flow cytometry in A549 cancer cells treated with complex 2 at different concentrations and complex 2 in the presence of NADH (400 µg/mL) at 2.8 µM. Data are quoted as mean ± SD of three replicates.

As NADPH oxidase is one of the main sources of ROS,<sup>46,47</sup> the effect of complex 2 on NOX4 was subsequently tested. Studies have shown that vast amounts of ROS were generated through the activation of the membrane-associated ROS-producing enzyme NADPH oxidase (NOX).<sup>48</sup> The results display that the expression of NOX4 was significantly enhanced after complex 2 (2.8 µM) treatment for 24 h, suggesting that 2-induced ROS generation in A549 cells was mediated by activating NOX4 (Figure S11).

The cytotoxicity induced by anticancer drugs could be associated with arresting cell cycle. The effects of 1 and 2 on cell cycle distribution were investigated by flow cytometry analysis (Figure S12 and Table S13). The percentages of A549 cells have a small increase in the S phase from 25.5 to 31.9%, indicating that 1 has a weak disturbance at the S phase of the

cell cycle, and that **2** disturbed the G<sub>1</sub> phase that increased 8.9%. The results indicate that negligible cycle arrest is not the cause of the difference in cell death caused by complexes **1** and **2**.

## CONCLUSION

In summary, we have synthesized and characterized two ferrocenyl–triphenyltin complexes acting as lysosome-targeting multifunctional platforms for anticancer therapy agents. Subtle structural changes lead to a significant impact on the cytotoxicity; **2** displayed higher cytotoxicity than **1** and cisplatin against A549, HeLa, HepG2, and GL261 cells. The results observed in the cyclic voltammograms and reaction with GSH for complexes **1** and **2** further confirmed that complex **1** showed favorable redox property but might lose anticancer effect by undergoing reaction with GSH. As an effective catalyst, **2** could convert NADH to NAD<sup>+</sup> through transfer hydrogenation reactions. NADH plays a significantly role in the loss of MMP and inducing ROS generation. Complex **2** could consume NADH in the cells, causing a decrease in mitochondrial membrane potential, have a significantly influence on ROS, and ultimately leading to cell death. The results of caspase-3 activation and cytoplasmic vacuolation karyorrhexis induced by **2** revealed that the A549 cell line might undergo cell death primarily mediated by apoptosis and oncosis; however, **1** cannot reproduce this effect. Taken together, various anticancer mechanism tests showed that complex **2** had good activity, which gives it more potential for evolution as new bioimaging and anticancer agents.

## MATERIALS AND INSTRUMENTATION

Unless otherwise noted, all manipulations were performed using standard Schlenk tube techniques under nitrogen atmosphere. The reagents ferrocenealdehyde (≥98.0%), acetylferrocene (≥97.0%), hydrazine hydrate (≥50%), Ph<sub>3</sub>SnCl (≥60%), and propionic acid hydrazine were purchased from Sigma-Aldrich. For the biological experiments, Hoechst 33342 (apoptosis and epigenetic company), 3-methyladenine (apoptosis and epigenetic company), cycloheximide, leupeptin, necrostatin-1, carbonyl cyanide *m*-chlorophenylhydrazone (CCCP), Z-VAD-FMK, and cleaved caspase-3 were purchased from Apoptosis and Epigenetics Company. MTDR (Life Technologies), LTDR (Life Technologies), MTT (3-(4,5-dimethylthiazol-2-yl)-2,5-diphenyltetrazolium bromide, Sigma-Aldrich), Annexin V-FITC Apoptosis Detection Kit (Sigma-Aldrich), JC-1 (Sigma-Aldrich), and PI (Sigma-Aldrich) are all used as received. EDTA (30 mM) was purchased from TaKaRa Biotechnology (Dalian, China). DMEM medium, fetal bovine serum, penicillin/streptomycin mixture, trypsin/EDTA, and PBS were purchased from Sangon Biotech. Testing compounds were dissolved in DMSO and diluted with the tissue culture medium before use.

## SYNTHETIC PROCEDURES

The synthesis of new ferrocenyl–organotin compounds is shown in Scheme 1.

**Synthesis of β-Methoxycarbonyl Ethyl Triphenyltin (S1).** S1 was prepared according to literature methods.<sup>28</sup>

**Synthesis of β-Hydrazinocarbonyl Ethyl Triphenyltin (S2).** S1 (2.0 g, 4.5 mmol) and methanol (30 mL) were added into a 250 mL three-necked bottle under N<sub>2</sub>, followed by stirring and heating to ebullience for 20 min. Hydrazine hydrate (50%, 30 mL) was added dropwise to above solution at 80 °C. The reaction was not stopped until S1 was consumed completely (monitored by thin-layer chromatography). Crude product was isolated by filtration and recrystallized from 60 mL of mixtures of chloroform and petroleum ether (*v/v* = 1:1) to obtain a colorless acicular crystal. Yield: 80.1%. mp, 144.2–144.5 °C. <sup>1</sup>H NMR (500 MHz, CDCl<sub>3</sub>) δ 7.56 (dt, *J* =

5.7, 2.6 Hz, 6H), 7.38–7.35 (m, 9H), 2.50 (t, *J* = 7.8 Hz, 2H), 1.67 (t, *J* = 7.8 Hz, 2H); ESI-MS (*m/z*): [M + Na]<sup>+</sup> Calcd for C<sub>21</sub>H<sub>22</sub>N<sub>2</sub>O<sub>2</sub>Sn: 461.08. Found 461.25.

### Synthesis of Ferrocenyl–Organotin Compounds (1 and 2).

The β-hydrazinocarbonyl ethyl triphenyltin (S2, 2.0 g, 4.3 mmol) and ferrocene derivatives (4.5 mmol) was dissolved in methanol in a dry round-bottomed flask and refluxed for 24 h. The progress of reaction was monitored by TLC. After complete conversion, methanol was removed under reduced pressure and product was dissolved in dichloromethane and filtered through Celite filtration funnel and recrystallized by slow diffusion of *n*-hexane in a concentrated solution of the compound in dichloromethane to obtain the corresponding complexes (**1** and **2**)

**1:** yield: 70.5%. <sup>1</sup>H NMR (500 MHz, CDCl<sub>3</sub>) δ 9.15 (s, 1H), 7.61 (dd, *J* = 6.3, 2.9 Hz, 5H), 7.36 (dd, *J* = 4.8, 1.7 Hz, 10H), 4.46–4.44 (m, 2H), 4.34–4.32 (m, 2H), 4.12 (s, 5H), 3.06 (t, *J* = 7.9 Hz, 2H), 1.73 (t, *J* = 7.9 Hz, 2H). Anal. Calcd: C, 60.70; H, 4.78; N, 4.42. Found: C, 60.74; H, 4.72; N, 4.43. ESI-MS (*m/z*): [M – Ph]<sup>+</sup> Calcd for C<sub>32</sub>H<sub>30</sub>FeN<sub>2</sub>O<sub>2</sub>Sn: 634.07. Found: 556.89.

**2:** yield: 65.3%. <sup>1</sup>H NMR (500 MHz, CDCl<sub>3</sub>) δ 8.71 (s, 1H), 8.49 (s, 1H), 7.84–7.73 (m, 6H), 7.44–7.31 (m, 9H), 4.61–4.57 (m, 2H), 4.41–4.38 (m, 2H), 4.16 (d, *J* = 5.2 Hz, 5H), 3.24 (dd, *J* = 13.1, 5.4 Hz, 2H), 2.10 (s, 3H), 1.81 (t, *J* = 7.7 Hz, 2H). Anal. Calcd: C, 61.24; H, 4.98; N, 4.33. Found: C, 61.26; H, 4.94; N, 4.43. ESI-MS (*m/z*): [M – Ph]<sup>+</sup> Calcd for C<sub>33</sub>H<sub>33</sub>FeN<sub>2</sub>O<sub>2</sub>Sn: 648.09. Found: 570.90.

L1 and L2 were synthesized by propionic acid hydrazine and ferrocene derivatives using the same methods of ferrocenyl–organotin compounds (Scheme S1).

**L1:** yield: 75%. <sup>1</sup>H NMR (500 MHz, DMSO) δ 10.92 (d, *J* = 46.8 Hz, 1H), 7.89 (d, *J* = 99.0 Hz, 2H), 4.59 (d, *J* = 7.3 Hz, 2H), 4.40 (d, *J* = 13.3 Hz, 2H), 4.20 (d, *J* = 4.5 Hz, 4H), 2.14 (t, *J* = 11.3 Hz, 1H), 1.05 (dd, *J* = 12.6, 7.5 Hz, 3H).

**L2:** yield: 80%. <sup>1</sup>H NMR (500 MHz, DMSO) δ 10.04 (d, *J* = 28.1 Hz, 1H), 4.58 (d, *J* = 23.3 Hz, 2H), 4.35 (d, *J* = 11.7 Hz, 2H), 4.17 (d, *J* = 8.1 Hz, 4H), 2.58–2.54 (m, 1H), 2.25 (dd, *J* = 14.8, 7.3 Hz, 1H), 2.12 (d, *J* = 10.2 Hz, 3H), 1.05 (t, *J* = 7.5 Hz, 3H).

## ASSOCIATED CONTENT

### Supporting Information

The Supporting Information is available free of charge on the ACS Publications website at DOI: 10.1021/acs.inorgchem.8b03305.

Experimental section, design strategy, stability monitored by UV–vis spectra, <sup>1</sup>H NMR spectra, electrostatic potential models, flow cytometry results, confocal microscopy images, cell cycle arrest results, crystallographic data, selected bond lengths and angles, growth inhibition, apoptosis, and caspase 3 activity results, MMP data, ROS induction, cell cycle analysis (PDF)

### Accession Codes

CCDC 1843945 contains the supplementary crystallographic data for this paper. These data can be obtained free of charge via [www.ccdc.cam.ac.uk/data\\_request/cif](http://www.ccdc.cam.ac.uk/data_request/cif), or by emailing [data\\_request@ccdc.cam.ac.uk](mailto:data_request@ccdc.cam.ac.uk), or by contacting The Cambridge Crystallographic Data Centre, 12 Union Road, Cambridge CB2 1EZ, UK; fax: +44 1223 336033.

## AUTHOR INFORMATION

### Corresponding Authors

\*E-mail: [chemlxc@163.com](mailto:chemlxc@163.com) (X.L.).

\*E-mail: [liuzheqd@163.com](mailto:liuzheqd@163.com) (Z.L.).

### ORCID

Xicheng Liu: 0000-0002-5932-7206

Zhe Liu: 0000-0001-5796-4335

## Notes

The authors declare no competing financial interest.

## ■ ACKNOWLEDGMENTS

We thank the University Research Development Program of Shandong Province (J18KA082), the National Natural Science Foundation of China (Grant No. 21671118) and the Taishan Scholars Program for support.

## ■ REFERENCES

- (1) Biot, C.; François, N.; Maciejewski, L.; Brocard, J.; Poulain, D. Synthesis and antifungal activity of a ferrocene–fluconazole analogue. *Bioorg. Med. Chem. Lett.* **2000**, *10*, 839–841.
- (2) Li, S.; Wang, Z.; Wei, Y.; Wu, C.; Gao, S.; Jiang, H.; Zhao, X.; Yan, H.; Wang, X. Antimicrobial activity of a ferrocene-substituted carborene derivative targeting multidrug-resistant infection. *Biomaterials* **2013**, *34*, 902–911.
- (3) Quirante, J.; Dubar, F.; González, A.; Lopez, C.; Cascante, M.; Cortés, R.; Forfar, I.; Pradines, B.; Biot, C. Ferrocene–indole hybrids for cancer and malaria therapy. *J. Organomet. Chem.* **2011**, *696*, 1011–1017.
- (4) Mahmoud, K. A.; Luong, J. H. T. Impedance method for detecting HIV-1 protease and screening for its inhibitors using ferrocene–peptide conjugate/Au nanoparticle/single-walled carbon nanotube modified electrode. *Anal. Chem.* **2008**, *80*, 7056–7062.
- (5) Hillard, E.; Vessières, A.; Thouin, L.; Jaouen, G.; Amatore, C. Ferrocene-mediated proton-coupled electron transfer in a series of ferrocifen-type breast-cancer drug candidates. *Angew. Chem., Int. Ed.* **2006**, *45*, 285–290.
- (6) Ornelas, C. Application of ferrocene and its derivatives in cancer research. *New J. Chem.* **2011**, *35*, 1973–1985.
- (7) Liu, X. C.; Tang, Y. H.; He, X. D.; Ge, X. X.; Liu, J.; Meng, X. Y.; Shao, M. X.; Jin, Y. M.; Tian, L. J.; Liu, Z. Triphenyltin(IV) acylhydrazone compounds: Synthesis, structure and bioactivity. *J. Inorg. Biochem.* **2019**, *191*, 194–202.
- (8) Arjmand, F.; Parveen, S.; Tabassum, S.; Pettinari, C. Organo-tin antitumor compounds: Their present status in drug development and future perspectives. *Inorg. Chim. Acta* **2014**, *423*, 26–37.
- (9) Basu Baul, T. S.; Dutta, D.; Duthie, A.; Rocha, B. G. M.; Guedes da Silva, M. F. C.; Saurav, S.; Manna, S. K. Syntheses, structural snapshots, solution redox properties, and cytotoxic performances of designated ferrocene scaffolds appended with organostannyl(IV) benzoates en route for human hepatic carcinoma. *Organometallics* **2018**, *37*, 2961–2979.
- (10) Girasolo, M. A.; Attanzio, A.; Sabatino, P.; Tesoriere, L.; Rubino, S.; Stocco, G. Organotin(IV) derivatives with 5,7-disubstituted-1,2,4-triazolo[1,5-a]pyrimidine and their cytotoxic activities: The importance of being conformers. *Inorg. Chim. Acta* **2014**, *423*, 168–176.
- (11) Gielen, M.; Davies, A. G.; Pannell, K.; Tiekink, E. *Tin Chemistry: Fundamentals, Frontiers, and Applications*; John Wiley & Sons, Ltd.: Wiley, 2008.
- (12) Berger, F.; Ramírez-Hernández, M. a. H.; Ziegler, M. The new life of a centenarian: Signalling functions of NAD(P). *Trends Biochem. Sci.* **2004**, *29*, 111–118.
- (13) Virág, L.; Szabó, C. The therapeutic potential of poly(ADP-Ribose) polymerase inhibitors. *Pharmacol. Rev.* **2002**, *54*, 375–429.
- (14) Ying, W.; Garnier, P.; Swanson, R. A. NAD<sup>+</sup> repletion prevents PARP-1-induced glycolytic blockade and cell death in cultured mouse astrocytes. *Biochem. Biophys. Res. Commun.* **2003**, *308*, 809–813.
- (15) Ying, W.; Alano, C. C.; Garnier, P.; Swanson, R. A. NAD<sup>+</sup> as a metabolic link between DNA damage and cell death. *J. Neurosci. Res.* **2005**, *79*, 216–223.
- (16) Ying, W. NAD<sup>+</sup> and NADH in brain functions, brain diseases and brain aging. *Front. Biosci., Landmark Ed.* **2007**, *12*, 1863–1888.
- (17) Ying, W. NAD<sup>+</sup>/NADH and NADP<sup>+</sup>/NADPH in cellular functions and cell death: Regulation and biological consequences. *Antioxid. Redox Signaling* **2008**, *10*, 179–206.
- (18) Shimada, H.; Hirai, K.-I.; Simamura, E.; Pan, J. Mitochondrial NADH–quinone oxidoreductase of the outer membrane is responsible for paraquat cytotoxicity in rat livers. *Arch. Biochem. Biophys.* **1998**, *351*, 75–81.
- (19) Zhao, Y.; Hu, Q.; Cheng, F.; Su, N.; Wang, A.; Zou, Y.; Hu, H.; Chen, X.; Zhou, H.-M.; Huang, X.; Yang, K.; Zhu, Q.; Wang, X.; Yi, J.; Zhu, L.; Qian, X.; Chen, L.; Tang, Y.; Loscalzo, J.; Yang, Y. SoNar, a highly responsive NAD<sup>+</sup>/NADH sensor, allows high-throughput metabolic screening of anti-tumor agents. *Cell Metab.* **2015**, *21*, 777–789.
- (20) Li, J.; Tian, M.; Tian, Z.; Zhang, S.; Yan, C.; Shao, C.; Liu, Z. Half-sandwich iridium(III) and ruthenium(II) complexes containing P<sup>+</sup>P<sup>-</sup>-chelating ligands: A new class of potent anticancer agents with unusual redox features. *Inorg. Chem.* **2018**, *57*, 1705–1716.
- (21) Li, J.; Guo, L.; Tian, Z.; Tian, M.; Zhang, S.; Xu, K.; Qian, Y.; Liu, Z. Novel half-sandwich iridium(III) imino-pyridyl complexes showing remarkable in vitro anticancer activity. *Dalton Trans* **2017**, *46*, 15520–15534.
- (22) Feng, Z.; Wang, H.; Wang, S.; Zhang, Q.; Zhang, X.; Rodal, A. A.; Xu, B. Enzymatic assemblies disrupt the membrane and target endoplasmic reticulum for selective cancer cell death. *J. Am. Chem. Soc.* **2018**, *140*, 9566–9573.
- (23) Zhu, H.; Fan, J.; Du, J.; Peng, X. Fluorescent probes for sensing and imaging within specific cellular organelles. *Acc. Chem. Res.* **2016**, *49*, 2115–2126.
- (24) Petersen, N. H. T.; Olsen, O. D.; Groth-Pedersen, L.; Ellegaard, A.-M.; Bilgin, M.; Redmer, S.; Ostenfeld, M. S.; Ulanet, D.; Dovmark, T. H.; Lønborg, A.; et al. Transformation-associated changes in sphingolipid metabolism sensitize cells to lysosomal cell death induced by inhibitors of acid sphingomyelinase. *Cancer Cell* **2013**, *24*, 379–393.
- (25) Daum, S.; Reshetnikov, M. S. V.; Sisa, M.; Dumych, T.; Lootsik, M. D.; Bilyy, R.; Bila, E.; Janko, C.; Alexiou, C.; Herrmann, M.; et al. Lysosome-targeting amplifiers of reactive oxygen species as anticancer prodrugs. *Angew. Chem., Int. Ed.* **2017**, *56*, 15545–15549.
- (26) Zhang, P.; Wang, Y.; Qiu, K.; Zhao, Z.; Hu, R.; He, C.; Zhang, Q.; Chao, H. A NIR phosphorescent osmium(II) complex as a lysosome tracking reagent and photodynamic therapeutic agent. *Chem. Commun.* **2017**, *53*, 12341–12344.
- (27) Grossi, M.; Morgunova, M.; Cheung, S.; Scholz, D.; Conroy, E.; Terrile, M.; Panarella, A.; Simpson, J. C.; Gallagher, W. M.; O’Shea, D. F. Lysosome triggered near-infrared fluorescence imaging of cellular trafficking processes in real time. *Nat. Commun.* **2016**, *7*, 10855–10866.
- (28) Appel, A.; Kober, C.; Neumann, C.; Nöth, H.; Schmidt, M.; Storch, W. Synthesis and structure of tris(trialkylstannyl)- and tris(dialkylhalostannyl)amines; stabilization of the Sn3N skeleton by intramolecular Sn–X–Sn bridges. *Chem. Ber.* **1996**, *129*, 175–189.
- (29) Liu, T.; Lai, L.; Song, Z.; Chen, T. A sequentially triggered nanosystem for precise drug delivery and simultaneous inhibition of cancer growth, migration, and invasion. *Adv. Funct. Mater.* **2016**, *26*, 7775–7790.
- (30) Santidrian, A. F.; Matsuno-Yagi, A.; Ritland, M.; Seo, B. B.; LeBoeuf, S. E.; Gay, L. J.; Yagi, T.; Felding-Habermann, B. Mitochondrial complex I activity and NAD<sup>+</sup>/NADH balance regulate breast cancer progression. *J. Clin. Invest.* **2013**, *123*, 1068–1081.
- (31) Ma, K.; Fu, D.; Liu, Y.; Dai, R.; Yu, D.; Guo, Z.; Cui, C.; Wang, L.; Xu, J.; Mao, C. Cancer cell targeting, controlled drug release and intracellular fate of biomimetic membrane-encapsulated drug-loaded nano-graphene oxide nanohybrids. *J. Mater. Chem. B* **2018**, *6*, 5080–5090.
- (32) He, L.; Li, Y.; Tan, C. P.; Ye, R. R.; Chen, M. H.; Cao, J. J.; Ji, L. N.; Mao, Z. W. Cyclometalated iridium(III) complexes as lysosome-targeted photodynamic anticancer and real-time tracking agents. *Chem. Sci.* **2015**, *6*, 5409–5418.
- (33) Liu, L.; Zhang, Z.; Xing, D. Cell death via mitochondrial apoptotic pathway due to activation of Bax by lysosomal photo-damage. *Free Radical Biol. Med.* **2011**, *51*, 53–68.

(34) Kumar, R.; Chauhan, A.; Jha, S. K.; Kuanr, B. K. Localized cancer treatment by radio-frequency hyperthermia using magnetic nanoparticles immobilized on graphene oxide: from novel synthesis to in vitro studies. *J. Mater. Chem. B* **2018**, *6*, 5385–5399.

(35) Petit, P. X.; Gendron, M.-C.; Schrantz, N.; Métivier, D.; Kroemer, G.; Maciorowska, Z.; Sureau, F.; Koester, S. Oxidation of pyridine nucleotides during Fas- and ceramide-induced apoptosis in Jurkat cells: correlation with changes in mitochondria, glutathione depletion, intracellular acidification and caspase 3 activation. *Biochem. J.* **2001**, *353*, 357–367.

(36) Li, Y.; Tan, C.-P.; Zhang, W.; He, L.; Ji, L.-N.; Mao, Z.-W. Phosphorescent iridium(III)-bis-*N*-heterocyclic carbene complexes as mitochondria-targeted theranostic and photodynamic anticancer agents. *Biomaterials* **2015**, *39*, 95–104.

(37) Li, N.; Yu, L.; Wang, J.; Gao, X.; Chen, Y.; Pan, W.; Tang, B. A mitochondria-targeted nanoradiosensitizer activating reactive oxygen species burst for enhanced radiation therapy. *Chem. Sci.* **2018**, *9*, 3159–3164.

(38) Sun, Y.; Yu, J.; Liu, X.; Zhang, C.; Cao, J.; Li, G.; Liu, X.; Chen, Y.; Huang, H. Oncosis-like cell death is induced by berberine through ERK1/2-mediated impairment of mitochondrial aerobic respiration in gliomas. *Biomed. Pharmacother.* **2018**, *102*, 699–710.

(39) Majno, G.; Joris, I. Apoptosis, oncosis, and necrosis. An overview of cell death. *Am. J. Pathology* **1995**, *146*, 3–15.

(40) Jing, Y.; Cao, Q.; Hao, L.; Yang, G. G.; Hu, W.-L.; Ji, L.-N.; Mao, Z. W. A self-assessed photosensitizer: inducing and dual-modal phosphorescence imaging of mitochondria oxidative stress. *Chem. Commun.* **2018**, *54*, 271–274.

(41) La Piana, G.; Marzulli, D.; Gorgoglione, V.; Lofrumento, N. E. Porin and cytochrome oxidase containing contact sites involved in the oxidation of cytosolic NADH. *Arch. Biochem. Biophys.* **2005**, *436*, 91–100.

(42) Marzulli, D.; La Piana, G.; Fransvea, E.; Lofrumento, N. E. Modulation of cytochrome *c*-mediated extramitochondrial NADH oxidation by contact site density. *Biochem. Biophys. Res. Commun.* **1999**, *259*, 325–330.

(43) Sivakumar, P.; Lee, M.; Kim, Y.-S.; Shim, M. S. Photo-triggered antibacterial and anticancer activities of zinc oxide nanoparticles. *J. Mater. Chem. B* **2018**, *6*, 4852–4871.

(44) Starkov, A. A.; Fiskum, G.; Chinopoulos, C.; Lorenzo, B. J.; Browne, S. E.; Patel, M. S.; Beal, M. F. Mitochondrial  $\alpha$ -ketoglutarate dehydrogenase complex generates reactive oxygen species. *J. Neurosci.* **2004**, *24*, 7779–7788.

(45) Zhang, Z.; Blake, D. R.; Stevens, C. R.; Kanuler, J. M.; Ward, P. G.; Symons, M. C. R.; Benboubetra, M.; Harrison, R. A reappraisal of xanthine dehydrogenase and oxidase in hypoxic reperfusion injury: the role of NADH as an electron donor. *Free Radical Res.* **1998**, *28*, 151–164.

(46) Ren, G.; Luo, W.; Sun, W.; Niu, Y.; Ma, D.-L.; Leung, C.-H.; Wang, Y.; Lu, J.-J.; Chen, X. Psoralidin induced reactive oxygen species (ROS)-dependent DNA damage and protective autophagy mediated by NOX4 in breast cancer cells. *Phytomedicine* **2016**, *23*, 939–947.

(47) Ma, G.; Luo, W.; Lu, J.; Ma, D.-L.; Leung, C.-H.; Wang, Y.; Chen, X. Cucurbitacin E induces caspase-dependent apoptosis and protective autophagy mediated by ROS in lung cancer cells. *Chem.-Biol. Interact.* **2016**, *253*, 1–9.

(48) Trachootham, D.; Alexandre, J.; Huang, P. Targeting cancer cells by ROS-mediated mechanisms: a radical therapeutic approach? *Nat. Rev. Drug Discovery* **2009**, *8*, 579–591.